

Coexistence of carbonyl and ether groups on oxygen-terminated (110)-oriented diamond surfaces

Shayantan Chaudhuri^{1,2}, Samuel J. Hall^{1,3}, Benedikt P. Klein^{1,4}, Marc Walker⁵, Andrew J. Logsdail⁶, Julie V. Macpherson¹✉ & Reinhard J. Maurer¹✉

Diamond-based materials have unique properties that are exploited in many electrochemical, optical, thermal, and quantum applications. When grown via chemical vapor deposition (CVD), the growth rate of the (110) face is typically much faster than the other two dominant crystallographic orientations, (111) and (100). As such, achieving sufficiently large-area and high-quality (110)-oriented crystals is challenging and typically requires post-growth processing of the surface. Whilst CVD growth confers hydrogen terminations on the diamond surface, the majority of post-growth processing procedures render the surface oxygen-terminated, which in turn impacts the surface properties of the material. Here, we determine the oxygenation state of the (110) surface using a combination of density functional theory calculations and X-ray photoelectron spectroscopy experiments. We show that in the 0–1000 K temperature range, the phase diagram of the (110) surface is dominated by a highly stable phase of coexisting and adjacent carbonyl and ether groups, while the stability of peroxide groups increases at low temperatures and high pressures. We propose a mechanism for the formation of the hybrid carbonyl-ether phase and rationalize its high stability. We further corroborate our findings by comparing simulated core-level binding energies with experimental X-ray photoelectron spectroscopy data on the highest-quality (110)-oriented diamond crystal surface reported to date.

¹Department of Chemistry, University of Warwick, Coventry CV4 7AL, UK. ²Centre for Doctoral Training in Diamond Science and Technology, University of Warwick, Coventry CV4 7AL, UK. ³Centre for Doctoral Training in Molecular Analytical Science, University of Warwick, Coventry CV4 7AL, UK. ⁴Diamond Light Source, Harwell Science and Innovation Campus, Didcot OX11 0DE, UK. ⁵Department of Physics, University of Warwick, Coventry CV4 7AL, UK. ⁶Cardiff Catalysis Institute, Cardiff University, Cardiff CF10 3AT, UK. ✉email: j.macpherson@warwick.ac.uk; r.maurer@warwick.ac.uk

Diamond is a material that possesses numerous extreme properties such as the highest hardness¹, thermal conductivity², and Debye temperature³ of any material, and thus has found use in a variety of fields. For many technological applications, the most common approach to growing diamond is via the process of chemical vapor deposition (CVD)⁴. Whilst high pressure, high temperature (HPHT) synthesis has also found use, it can be difficult to control impurity content via HPHT⁵, hence the preferred use of CVD-grown crystals in many technological applications⁶. For large-area applications, it is much cheaper to grow polycrystalline diamond (PCD) than single-crystal diamond (SCD); PCD has numerous industrial applications, such as in thermal management⁷ and electrochemistry. In the latter case, highly boron-doped diamond (BDD) has been used as an electrode material⁸ for a variety of sensing applications, as well as waste water treatment and chemical disinfection⁹.

Depending on CVD growth conditions, the (110) facet typically grows much faster than the (111) and (100) surfaces, and therefore outgrows the other two primary crystallographic orientations^{10–12}. In this regard, the (110) facet thus serves as a useful model of the more reactive sites during diamond growth¹³. In polycrystalline material, the (110) facets can be revealed by mechanically polishing to a surface roughness where the surface is predominantly (110)-textured. This has been experimentally demonstrated using electron backscatter diffraction¹⁴ and scanning transmission electron microscopy¹⁵. Such surfaces have found practical use in electrochemical applications, where the PCD material can be treated as a textured surface with a dominant (110) orientation^{14,15}. (110)-oriented SCDs also currently find applications in photonics¹⁶. With SCD, growth of the required crystal face is achieved by using a single crystal substrate of the same orientation for epitaxial growth¹⁷ or by laser cutting along the required axis post-growth. As the diamond grows thicker, or the growth substrate moves away from atomic smoothness, achieving monocrystallinity becomes more challenging^{11,17}. This is especially true of the (110) orientation, where the crystal face decreases in size as the crystal gets thicker¹⁸.

Whilst diamond surfaces are usually hydrogen-terminated after CVD growth¹⁹, mechanical polishing or chemical cleaning, typically using strong oxidizing agents, leaves the surface oxygen-terminated, which confers hydrophilicity^{20,21} and a positive electron affinity²². Even if untreated, the hydrogen-terminated surface can gradually oxidize over time in air^{23,24}. Oxygen terminations can reduce surface electrical conductivity²³, increase capacitance²⁵, and impact the electron-transfer kinetics of inner-sphere electrochemical reactions on BDD electrodes⁸. Oxygen terminations also increase the density of negatively-charged nitrogen-vacancy centers near the surface^{26,27} (that can arise from impurities in the CVD process^{4,19}), which have applications in photonics, quantum optics²⁸, and quantum computing^{29–31}. A detailed atomic-scale understanding of the surface termination and elementary surface composition of (110)-oriented diamond is therefore of vital importance.

The oxygenation state of the diamond (110) surface has not been extensively characterized, with previous studies primarily focusing on the (111) and (100) surfaces¹³. This is most likely due to the challenges associated with growing and preparing a (110)-oriented SCD surface with a large-enough area at a high-enough quality¹¹ (*vide infra*). Theoretical studies have identified the presence of carbonyl and ether functional groups on the diamond (111) and (100) surfaces^{32–42}. Experimental techniques, such as infrared (IR) and X-ray photoelectron spectroscopy (XPS), can be used to confirm the presence of different oxygenic moieties on diamond surfaces. For example, experimental studies on the (111)

and (100) surfaces indicate the presence of carbonyl and ether groups^{43–46} after the removal of loosely-bound compounds and organic contaminants. The few experimental studies that exist for the (110) surface are also interpreted in the context of a coexistence of carbonyl and ether groups^{13,47–49}, with peroxide groups being reported on the (110) surface at low temperatures using IR spectroscopy¹³. However, in two of these studies, the (110) surfaces were subjected to a hydrogen plasma treatment before analysis^{13,49}, which is known to induce the formation of (111) microfacets^{13,49,50}, compromising the (110) crystallinity of the surface. Makau and Derry only presented XPS data recorded at room temperature (RT), where the physisorbed contaminants may still be present and no details about the quality of the studied crystal were provided⁴⁷. In Baldwin et al.⁴⁸, the crystal was assumed to contain a mixture of (110) and (111) facets and a large number of step edges, with a measured surface roughness of 1 nm. These studies highlight the challenges of preparing high-quality (110) surfaces.

In this paper, we present a systematic characterization of the structure and stability of various oxygenic terminations of the diamond (110) surface. This is achieved through a combination of density functional theory (DFT)^{51,52} calculations and XPS experiments (at elevated temperatures) on an epitaxially CVD-grown (110)-oriented BDD substrate. The post-growth surface is polished to an average surface roughness and a root mean square roughness of 0.18 and 0.23 nm respectively, as was determined using atomic force microscopy (AFM). X-ray diffraction (XRD) and low-energy electron diffraction (LEED) did not indicate the presence of any other crystallographic orientations. We use *ab initio* atomistic thermodynamics^{53–55} based on DFT to establish a phase diagram of a large number of surface structures and identify the most stable oxygenation state of the (110) surface. The phase diagram of the (110) surface is dominated by highly stable coexistent carbonyl and ether groups, which is also corroborated by XPS measurements and simulations. This highly stable phase of adjacent carbonyl and ether groups satisfies all valencies and a simple mechanism connecting this structure to adsorbed molecular oxygen can be formulated. Individual surface carbonyls on the other hand would be unstable and lead to the creation of surface radicals that can induce further surface restructuring.

Results and discussion

Structure and stability of oxygen-terminated surfaces. An extensive computational structure search was performed to identify the atomically-flat oxygen-terminated (110) surfaces with the highest stabilities, varying both the termination and surface coverage of oxygen. Our search involved placing surface-terminal carbonyl/ketone (C=O), ether (C–O–C), peroxide (C–O–O–C), and hydroxy (C–OH) groups, as well as combinations thereof, on a diamond (110) surface slab and performing geometry optimizations. We consider 22 different optimized surface terminations, which are visualized along with their calculated adsorption energies and fractional oxygen surface coverages in Supplementary Table 1 in Supplementary Note 2. Table 1 summarizes the adsorption energies of the most stable phases, which are also depicted in Fig. 1; in both, three- and five-ring ethers are denoted as Ether₃ and Ether₅, respectively, and carbonyls are denoted as Keto groups. We find the most stable phases to contain carbonyl, ether, and peroxide functional groups, which agrees with existing experimental literature^{13,47–49}. In particular, phases containing coexistent carbonyl and ether groups appear to have the largest adsorption energy, with the $p(2 \times 1)$ Keto-Ether₅ phase having by far the largest E_{ads} and E_{ads}/A values of 3.03 eV atom⁻¹ and 0.34 eV Å⁻², respectively. The $p(2 \times 2)$ Keto-Ether₅ phase, a half-

coverage form of the $p(2 \times 1)$ Keto-Ether₅ phase, is the most stable phase at lower coverage.

Figure 1 shows the convex hull of the calculated free energy of adsorption, ΔG_{ads} , as a function of the gas-phase chemical potential of oxygen, $\Delta\mu_{\text{O}}$; a full free energy plot featuring all the phases can be found in Supplementary Fig. 1 in Supplementary Note 3. Here we consider the oxygenated surface to be in equilibrium with a gas phase of molecular oxygen at temperature and pressure conditions, (T, p) , that correspond to a certain chemical potential (for details see Methods section). The structure with the largest ΔG_{ads} value (note the inverted y -axis) is the most stable at the given $\Delta\mu_{\text{O}}$ value, and therefore (T, p) couple, and will be thermodynamically realized under these conditions (notwithstanding any kinetic barriers)^{53,55}. Over the shown range of $\Delta\mu_{\text{O}}$ values, the following three surface structures constitute the convex hull, i.e., they are the most thermodynamically stable under these conditions: the clean (110) surface, the $p(2 \times 1)$ Keto-Ether₅ and the $p(1 \times 1)$ Peroxide phases. The unterminated surface is the most stable configuration below $\Delta\mu_{\text{O}} = -3.03$ eV atom⁻¹. As $\Delta\mu_{\text{O}}$ increases further, the $p(2 \times 1)$ Keto-Ether₅ phase is the

most stable until $\Delta\mu_{\text{O}} = 0.29$ eV atom⁻¹. Above this, the $p(1 \times 1)$ Peroxide phase becomes the most stable configuration, which is to be expected as the free energy of oxygen adsorption increases with $\Delta\mu_{\text{O}}$. This results in an increase in the stability of oxygen-rich phases relative to oxygen-poor surfaces and the $p(1 \times 1)$ Peroxide phase possesses the maximal oxygen coverage. Visualizations of the clean surface, $p(2 \times 1)$ Keto-Ether₅ and $p(1 \times 1)$ Peroxide phases are given in Fig. 2.

The range of temperatures and pressures at which the most stable phases are realized can be seen in Fig. 3. Over the temperature range of 0–1000 K, at standard pressure, the $p(2 \times 1)$ Keto-Ether₅ phase is the most stable configuration, and therefore is expected at standard atmospheric conditions. The unterminated surface is the most stable phase at higher temperatures ($T > 1000$ K) and lower pressures ($p < 10^{-6}$ atm), which is expected as the stability of an oxygen ideal gas increases with increasing T and decreasing p . The $p(1 \times 1)$ Peroxide phase is the most stable phase at lower temperatures, with suprema ranging from around 60 K to around 100 K over the whole pressure range.

Previous experimental studies on the oxygenation state of the (110) surface provide evidence of oxygen species which broadly supports our findings. However, we note the caveat concerning the quality of the surfaces used in these studies^{13,47–49}. These studies report carbonyl and ether groups on the surface^{13,47–49}, while surface peroxide species are reported to exist at low temperatures (90 K)¹³. However, we note that the ab initio atomistic thermodynamics method does not consider any kinetic information, such as reaction barriers, that are likely to affect which phases are experimentally observed under which conditions. Vibrational contributions to ΔG_{ads} were also not considered here, comprising the vibrational entropy and enthalpy^{53,54}, which can shift the stability boundaries to some extent. We do not expect these contributions to affect the convex hull as the Keto-Ether₅ phases are significantly more stable than all other considered phases. As an additional note, the Perdew-Burke-Ernzerhof (PBE)⁵⁶ exchange-correlation (XC) functional, which has been used in this work, is known to underestimate adsorption energies and

Phase	$E_{\text{ads,A}}$ (eV Å ⁻²)	E_{ads} (eV atom ⁻¹)	Coverage (atoms nm ⁻²)
$p(1 \times 1)$ Peroxide	0.31	1.42	22.2
$p(2 \times 1)$ Keto-Ether ₅	0.34	3.03	11.1
$p(2 \times 1)$ Peroxide	0.23	2.04	11.1
$p(1 \times 1)$ Ether ₃	0.20	1.77	11.1
$p(1 \times 1)$ Ether ₅	0.17	1.52	11.1
$p(2 \times 2)$ Keto-Ether ₅	0.25	2.25	5.5
$p(2 \times 2)$ Peroxide	0.10	1.78	5.5

Energies are given as a function of surface area and per atomic adsorbate, as well as the associated surface coverage, for the most stable oxygen-terminated (110) surface phases. Entries are ordered from high to low oxygen surface coverage.

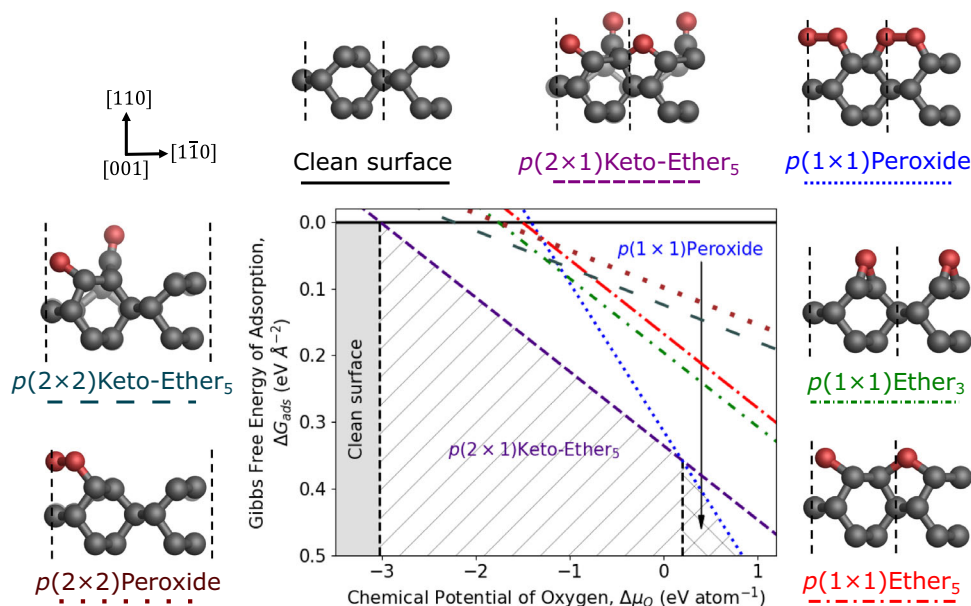


Fig. 1 Free energy plot of the most stable oxygen-terminated diamond (110) surface phases. The shaded region represents the convex hull of the free energy of adsorption, ΔG_{ads} . ΔG_{ads} is presented as a function of the chemical potential of oxygen, $\Delta\mu_{\text{O}}$, in the gas phase. The free energy of adsorption is shown for the most stable phases listed in Table 1. A full free energy plot of all phases can be seen in Supplementary Fig. 1. Orthographic ball-and-stick visualizations of the first three carbon layers of the phases are shown as viewed ‘front on’ from the [001] direction, with carbon and oxygen atoms shown in gray and red respectively. The unit cell outlines of the surrounding structures are shown in black dashed lines with surface axes also presented.

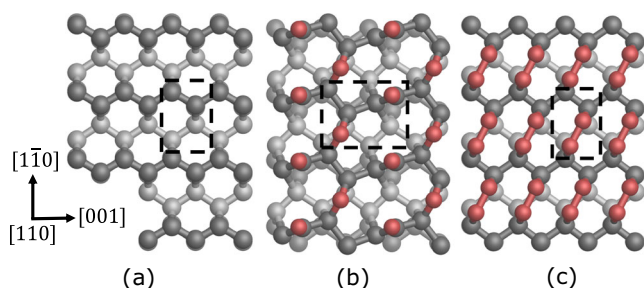


Fig. 2 Orthographic ball-and-stick visualizations of the three most stable oxygen-terminated diamond (110) surface phases. **a** Clean surface, **b** $p(2 \times 1)$ Keto-Ether₅, and **c** $p(1 \times 1)$ Peroxide, shown from the [110] direction as a 'top-down' view. Carbon and oxygen atoms are shown in gray and red respectively, and the unit cell outlines are shown with black dashed lines. Surface axes are also presented.

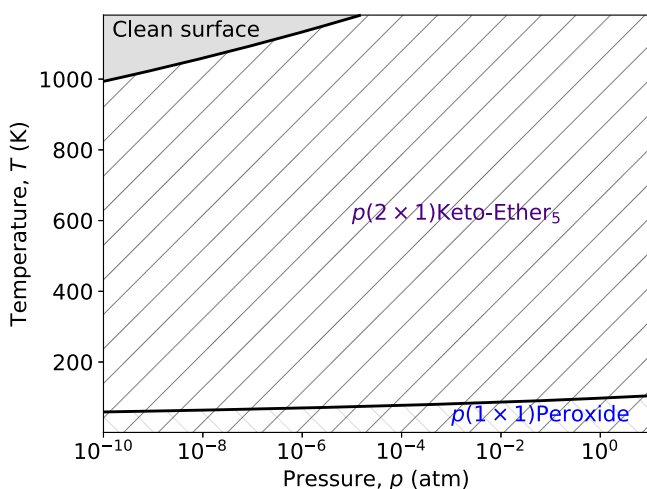


Fig. 3 Phase diagram of the oxygen-terminated diamond (110) surface. The diagram is presented as a function of both temperature, T , and pressure, p , and shows the three most stable oxygen-terminated diamond (110) surface phases.

overestimate adsorption distances in many cases^{57–59}. To assess the effect of the choice of XC functional, surface structures were reoptimized, and adsorption energies recalculated with different XC functionals^{60–64} for the $p(2 \times 1)$ Keto-Ether₅ and $p(1 \times 1)$ Peroxide phases. While we find that the absolute adsorption energy does depend on the XC functional, the ordering of the two phases and the significantly higher stability of the $p(2 \times 1)$ Keto-Ether₅ phase is confirmed as independent of the XC functional, as can be seen in Supplementary Table 2 in Supplementary Note 5. We, therefore, consider our findings to be robust with respect to the choice of XC functional.

In the following, we address the origin of the high stability of the Keto-Ether₅ phases. During the structure optimizations, the Keto-Ether₅ phases form spontaneously from manually-prepared peroxide structures aligned along the [110] direction. A schematic of the optimization mechanism is shown in Fig. 4. The initially-adsorbed peroxide forms two oxygen radicals, one of which is saturated by forming a carbonyl group at the expense of a carbon-carbon bond between the first and the second layer, while the other is stabilized by bridging the ridge to form a five-ring ether. The $p(2 \times 1)$ Keto-Ether₅ structure has been verified to be the most stable structure via a global structure search using the minima-hopping algorithm^{65–67}.

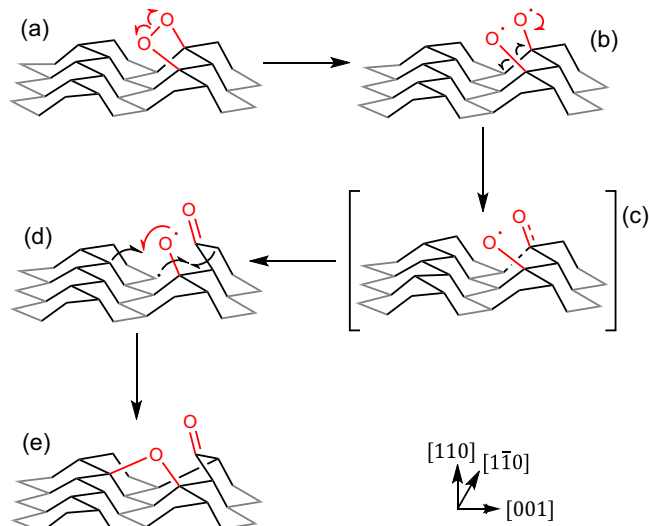


Fig. 4 Structural rearrangement during the formation of the $p(2 \times 1)$ Keto-Ether₅ phase. The initial peroxide termination is along the C-C ridge in the [110] direction. First, **a** the O-O bond breaks to form two oxygen radicals (O·), one of which then proceeds to form a double bond with a surface carbon atom (**b**). Due to the propensity of carbonyl groups to form trigonal planar structures, one of the C-C bonds in the tetrahedral diamond structure also breaks. Both processes are underway in the transition state (**c**). In order to form a stable structure, the remaining O· bridges over the surface ridge to form an ether group, allowing the carbon radical (C·) to bond with another carbon atom behind the carbonyl (**d**). The resulting structure is the $p(2 \times 1)$ Keto-Ether₅ phase (**e**). Surface axes are also presented.

To further understand the large adsorption energy of 3.03 eV atom⁻¹, we examine the structure of the $p(2 \times 1)$ Keto-Ether₅ phase against other surface phases by analyzing bond lengths and bond angles, and by comparing against valence shell electron pair repulsion (VSEPR) theory. In our calculations, we find that carbonyl groups seem to lead to some lattice distortion, with C-C=O bond angles of 123.2° and 125.0° in the $p(2 \times 1)$ Keto-Ether₅ phase, which indicates a more trigonal planar surface structure. Based on VSEPR theory, partial sp^2 hybridization has occurred in the surface carbon layers, which is consistent with partial graphitization and sp^2 hybridization in diamond^{68–71}. Further geometrical distortions can be seen by comparing carbon-oxygen bond lengths. Other surface terminations that feature ether, peroxide, or hydroxy surface groups seem to preserve the sp^3 hybridization of the carbon atoms, with a C-O bond length of typically around 1.45 Å, with the exception of 1.55 Å in Ether₅ phases; in comparison, the C=O bond length in the Keto-Ether₅ phases is 1.20 Å, shorter than the observed C-O bonds. The formation of the C=O bond pulls the respective carbon atom above the diamond surface plane, as can be seen in the Keto-Ether₅ structures shown in Fig. 1.

While C=O bonds are typically stronger than C-O bonds, individual surface carbonyl groups cannot be realized on a pristine (110) surface as they would require the breaking of C-C bonds, creating carbon radicals and leading to a substantial deformation of the surface. To circumvent that, another surface moiety such as an ether group must be present to saturate the carbon radicals and minimize the necessary deformation (Fig. 4). The adjacent carbonyl and ether functionalities in the Keto-Ether₅ phases possess such a high stability because their local pairing is able to balance the high adsorption energy from the carbonyl with low structural deformation in the surface. Taking the distorted surface

Table 2 Comparison of C 1s BE shifts for the Keto-Ether₅ phases with respect to the diamond bulk signal (Δ BE).

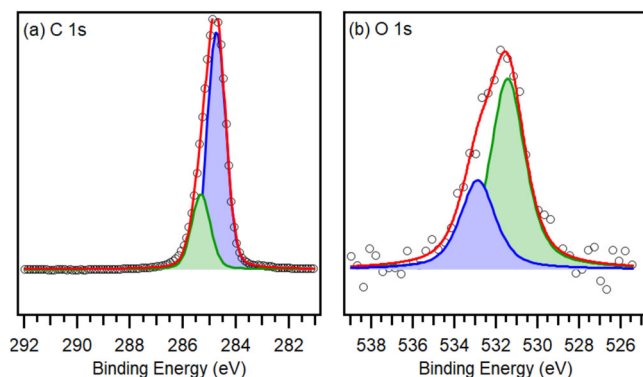
C 1s Δ BE (eV)					
Species	Simulation		Experiment		
	$p(2 \times 1)$	$p(2 \times 2)$	This Work	Baldwin ⁴⁸	Makau ⁴⁷
C=O	1.16	0.74	0.7	4.5	2.2
C-O-C	1.46	0.80	0.7	1.9	1.1
C-O-C	1.23	0.30	0.7	1.9	1.1

For the simulation of the ether moiety, two carbon BEs are given, one for each oxygen-bonded carbon atom. Our own experiments only show one peak in addition to the bulk diamond signal, while the literature reports two additional peaks at a much higher BE. See text for detailed discussion. The "Baldwin" and "Makau" columns refer to the Baldwin et al.⁴⁸ and Makau and Derry⁴⁷ studies, respectively.

Table 3 Comparison of the O 1s BE difference (Δ BE) for the Keto-Ether₅ phases.

O 1s Δ BE (eV)				
Simulation		Experiment		
$p(2 \times 1)$	$p(2 \times 2)$	This Work	Baldwin ⁴⁸	Makau ⁴⁷
1.00	1.31	1.5	2.1	1.7

The O 1s Δ BE is calculated as the difference between the BEs of the oxygen atoms involved in the carbonyl (C=O) and ether (C-O-C) functional groups. The experimental data reports the Δ BE between the two peaks in the corresponding O 1s spectra. The "Baldwin" and "Makau" columns refer to the Baldwin et al.⁴⁸ and Makau and Derry⁴⁷ studies respectively.

**Fig. 5 Experimental X-ray photoelectron spectra of the sample surface.**

a Carbon 1s (C 1s) spectrum and **b** oxygen 1s (O 1s) spectrum. Spectra were taken at normal emission after annealing the sample to 500 °C. The raw data, fit functions, and fitted peaks are shown using open circles, red lines, and shaded areas respectively.

slab upon adsorption of oxygen in the $p(2 \times 1)$ Keto-Ether₅ phase to be E_{slab} in Eq. 1, the E_{ads} value is recalculated to be 5.26 eV atom⁻¹. Therefore, the structural deformation penalty associated with adsorption is 2.23 eV atom⁻¹. Without the ether group, this deformation penalty would be much higher. The fact that the geometry optimization of an adsorbed peroxide leads to the formation of the Keto-Ether₅ phase, suggests that the pathway shown in Fig. 4 can be a viable oxidation mechanism of the diamond (110) surface.

X-ray photoemission signatures of oxygen and carbon species.

To connect our predicted structures with experimental data, the core-level binding energies (BEs) of the central carbon and

oxygen species in our DFT-based structures were simulated with the Delta Self-Consistent Field method⁷². We compare these simulations to results from our own experimental XPS measurements, as well as to those reported in literature^{47,48}. The DFT-based core-level simulations were performed for both cluster and periodic models. While periodic models allow for accurate calculation of the relative shifts between different species, their inherent properties mean that absolute BEs, which can be directly compared to experimental values, are only accessible in cluster calculations⁷². For both periodic and cluster calculations, the convergence behavior of the resulting BEs was carefully tested with respect to the unit cell size and cluster radius. All convergence tests are compiled in Supplementary Note 7, where Supplementary Fig. 7 shows the convergence behavior of the BEs for the $p(1 \times 1)$ Peroxide phase. In the case of the $p(2 \times 1)$ Keto-Ether₅ phase, the difference between the oxygen 1s (O 1s) BE for the carbonyl and ether groups is a good measure of convergence behavior. Supplementary Fig. 8 shows that both the cluster and periodic calculations converge to the same value (0.8 eV). We can therefore rule out finite-size and cell-charging effects from affecting the relative BE shifts obtained by our periodic calculations. The agreement between the cluster and periodic models also verifies that the terminating hydrogen species in the cluster model do not influence the XPS behavior of the central carbon and oxygen atoms. Therefore all BEs reported hereafter were obtained from the converged periodic surface models.

The simulation results for the core-electron BEs of the Keto-Ether₅ phase in two coverages, $p(2 \times 1)$ and $p(2 \times 2)$, are detailed in Tables 2 and 3, where they are compared to experimental XPS data, both from literature^{47,48} and from our own experiments. The tables compare relative BE shifts and differences between the different species. The carbon 1s (C 1s) BEs in Table 2 are presented as shifts with respect to the bulk carbon signal of the diamond surface, both for experiment and simulation. In the case of the O 1s data in Table 3, only the BE difference between the two oxygen species present in the different functional groups, carbonyl (C=O) and ether (C-O-C), are discussed.

As can be seen in Table 2, the calculated C 1s BEs for carbonyl and ether carbons are close together; in the lower-coverage $p(2 \times 2)$ phase, the C=O BE sits evenly between the two C-O-C carbons present in the structure. This result is in agreement with our own experiments, presented in Fig. 5, which shows the experimental C 1s and O 1s spectra recorded after annealing our sample surface to 500 °C. The C 1s spectrum in Fig. 5(a) is dominated by a main peak with a small shoulder at a higher BE, caused by a small peak partly underneath the main peak. The BE difference between the two peaks is 0.7 eV (0.6–0.9 eV). As can be seen in Fig. 5b, two species are present in the O 1s spectrum: the high BE peak corresponds to an ether moiety, while the low BE peak can be attributed to a carbonyl group. The relative shift between the two species is 1.5 eV (1.4–1.6 eV). The lower BE peak of the carbonyl has a higher intensity, with an intensity ratio of about 2:1. Therefore, both spectra can be fitted sufficiently using only two sub-peaks. The resulting experimental peak shifts between the two respective peaks are also included in Tables 2 and 3.

Contrary to both our calculations and experiments, data published in literature^{47,48} shows two additional oxygen-related peaks at much higher BE. We believe that this discrepancy, as discussed above, is due to both crystal quality and the lack of sample annealing prior to running XPS experiments. Even small concentrations of contaminants in the atmosphere that the sample is exposed to prior to measurement can lead to a high coverage of contaminants adsorbed on the surface; these contaminants will still be present after the sample is introduced into the vacuum chamber of the photoelectron spectrometer⁷³.

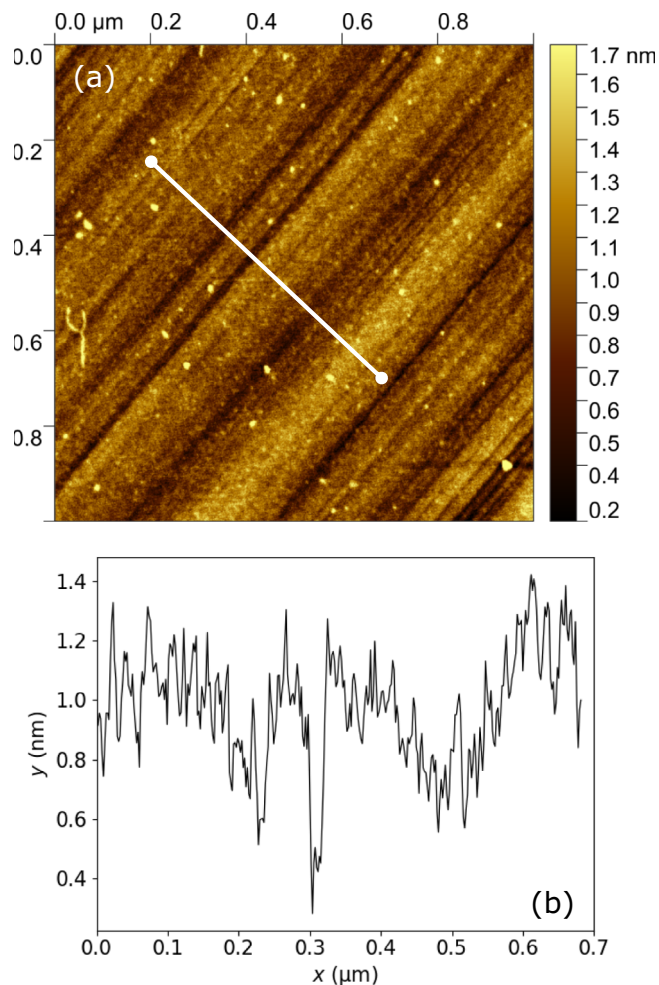


Fig. 6 Atomic force microscopy (AFM) of the (110)-oriented diamond sample surface. **a** $1.0 \times 1.0 \mu\text{m}^2$ AFM image and **b** the roughness profile of the white line in **(a)**. The average surface roughness and the root mean square roughness were found to be 0.18 and 0.23 nm respectively.

Contaminants can cause surface reactions, introduce additional signals into the O 1s region, and also show oxygen-related peaks in the C 1s region. Supporting our argument are our own XPS experiments, where a large quantity of contaminants were observed desorbing from the diamond surface when annealed, as shown in Supplementary Fig. 11); these contaminants were most probably adventitious non-diamond carbonaceous species such as hydrocarbons, CO-derivatives and other organic compounds^{74–77}. The spectra taken prior to sample annealing show a similar shape as the literature data, and also contain additional peaks at 1.5 and 4.1 eV above the bulk diamond peak, as is shown in Supplementary Fig. 11c in Supplementary Note 8.

Discussion. The simulated BEs of the lower coverage $p(2 \times 2)$ Keto-Ether₅ system are close to our experimental XPS data, while the higher coverage $p(2 \times 1)$ Keto-Ether₅ model shows a larger deviation from the experiment. We also observe good agreement between simulated O 1s BE differences for the low coverage structure and our own experiments (see Table 3). On the other hand, the simulations of the high coverage structure show deviations that cannot be reconciled with our experiments once the obvious surface contaminants are removed. We hypothesize that the larger deviations observed for the $p(2 \times 1)$ system might be due to the higher coverage structure being difficult to realize

for realistic surfaces under our experimental conditions as employed herein.

XRD and LEED experiments were performed to gather further information about the quality of our studied diamond (110) surface, the results of which are compiled in Supplementary Note 8. XRD measurements showed the sample surface to be orthogonal to the [110] direction (Supplementary Fig. 9), and the surface-sensitive LEED measurements showed a reflex pattern in agreement with the translational symmetry of a (110) surface^{50,78–80} (Supplementary Fig. 10). AFM measurements were also conducted to obtain information about the sample surface roughness and morphology. Figure 6 shows a typical $1.0 \times 1.0 \mu\text{m}^2$ image of the sample surface topography; S_a and S_q were found to be only 0.18 and 0.23 nm respectively, which is close to atomic smoothness. The small bright spots are associated with impurities ('dirt') on the surface. Repeated sonication of the crystal during the cleaning stage was found to decrease the small particle density and size. Our (110) surface is of higher quality than all others currently reported in literature^{13,47–50,78–81} for this challenging crystallographic growth orientation.

Using ab initio atomistic thermodynamics based on DFT, we have established a phase diagram of the most stable oxygen terminations of the diamond (110) surface. Within the 0–1000 K temperature range, the phase diagram is dominated by a highly stable phase of coexistent carbonyl and ether functional groups, while peroxide groups become more stable at low temperatures and high oxygen pressures, which is in agreement with existing experimental literature. Adjacent carbonyl and ether groups are observed, which as our calculations suggest, can form by a transition from an adsorbed peroxide structure. The high stability of the adjacent carbonyl and ether groups arises from cooperative effects that mitigate surface deformation and satisfy all valencies. Our findings are robust with respect to the XC functional. From the simulation of core-level BEs, we find that a lower coverage of this coexistent and adjacent carbonyl/ether phase produces core-level shifts in agreement with our experimental XPS data. While the experimental data does not agree with the simulation results for the most stable highest coverage, this could indicate that this coverage may not be able to be realized due to kinetic hindrance and coverage limitations on realistic surfaces. As the fastest growing major diamond facet, the (110) orientation is the one least studied in literature due to its associated growth challenges. However, in polished PCD applications, it is the dominant surface crystallography and has use in technological CVD diamond applications. Our combined theoretical and experimental analyses provide a much improved understanding of the oxygen-terminated diamond (110) surface, which has been lacking to-date. A better characterization of the chemical terminations of diamond-based materials is crucial to understanding elementary diamond growth and electrochemical surface processes.

Methods

Computational structure exploration. DFT^{51,52} calculations were conducted using the numeric atomic orbital FHI-aims^{82–86} software package, with calculations making use of the PBE⁵⁶ XC functional. Structures were constructed using the Atomic Simulation Environment⁶⁷; all structures were symmetric with oxygenic species terminating both the top and bottom of a seven-layer dipole-canceling diamond (110) slab. To account for cases where only partial oxidation of the (110) surface might occur, the following surface unit cells were optimized and studied: $p(1 \times 1)$, $p(2 \times 1)$, $p(1 \times 2)$, and $p(2 \times 2)$. The numeric atomic orbitals were represented using a 'tight' basis set⁸² and van der Waals effects were included through the pairwise long-range Tkatchenko-Scheffler dispersion correction method⁸⁷. Further self-consistency settings can be found in Supplementary Note 1.

To calculate the oxygen adsorption energy, E_{ads} , Eq. 1 was used:

$$E_{\text{ads}} = \frac{1}{N} (E_{\text{total}} - E_{\text{slab}} - NE_{\text{O}}) \quad (1)$$

where N is the number of oxygen atoms, E_{total} is the total energy of the terminated surface and E_{slab} is the energy of the surface onto which the oxygenic species is being adsorbed. The oxygen adsorbate energy, E_{O} , was calculated as half the total energy

of a free oxygen molecule (O_2), while for hydroxyl adsorbates, E_O was calculated as the difference between the energy of a free water molecule and half the energy of a free hydrogen molecule. The adsorption energy per unit cell surface area, E_{ads}/A , was calculated by multiplying E_{ads} by N/A . For simplicity, the absolute value of the adsorption energy was taken i.e., a positive value corresponds to an exothermic process. Convergence with respect to the seven-layered model was also established.

Using the calculated adsorption energies, we calculate the free energy of adsorption, ΔG_{ads} , for every termination as a function of the chemical potential of oxygen in the gas phase with Eq. 2. Here, we assume that the surface is in equilibrium with an oxygen atmosphere that behaves as an ideal gas. The chemical potential of oxygen, $\Delta\mu_O$, represents the ease of oxygen adsorption onto the surface^{53,55}:

$$\Delta G_{ads}(\Delta\mu_O) = \frac{N}{A}(\Delta\mu_O + E_{ads}), \quad (2)$$

We further express $\Delta\mu_O$ as a function of both temperature, T , and pressure, p , using Eq. 3⁵³:

$$\Delta\mu_O(T, p) = \Delta\mu_O(T, p^\ominus) + \frac{1}{2}k_B T \ln\left(\frac{p}{p^\ominus}\right), \quad (3)$$

where k_B is the Boltzmann constant and p^\ominus is standard pressure (1 atm). $\Delta\mu_O(T, p^\ominus)$ was calculated using a polynomial fit, as detailed in Supplementary Equation 1 in Supplementary Note 4, to data for O_2 in the NIST thermochemical tables⁸⁸.

Simulation of core-level BEs. XPS core-level BEs were calculated using the Delta Self-Consistent Field^{89,90} method by taking the energy difference between two self-consistent Kohn–Sham DFT calculations: the ground-state calculation and the excited core-hole-constrained calculation, where the population of an atom (either carbon or oxygen) was constrained to remove one electron. Both periodic and aperiodic core-hole calculations were performed using the PBE⁵⁶ XC functional. Periodic calculations were performed using the plane-wave pseudopotential (PP) CASTEP 18.1⁹¹ software package, with default on-the-fly generated ultrasoft PPs and a plane-wave cut-off of 650 eV. Here, the core-hole was localized through the generation of a modified PP with a core-hole included on the target atom. The energetic contribution of core electrons was accounted for via a correction term when calculating BEs between the ground and excited states⁹². Supercells of various sizes were constructed to systematically assess BE convergence and the role of finite size effects. Convergence with respect to the 7-layered model was also established. More information regarding the calculations can be found in Supplementary Note 7.

Aperiodic (or cluster) calculations were performed using FHI-aims^{82,83} with the `force_occupation_basis` keyword to constrain the core-hole, along with additional basis functions to better describe the core-states, as laid out by Kahk and Lischner (2019)⁹³. The aperiodic calculations were performed on hemispherical cluster models of various phases, cut from their parent periodic models using the Py-ChemShell⁹⁴ software package. Dangling bonds for all atoms were terminated with hydrogen species, though the XPS calculations were conducted on the central carbon and oxygen atoms. Using a Mulliken analysis⁹⁵, the density of states of each cluster was compared against its parent periodic model, details of which can be found in Supplementary Note 6. Cluster models, unlike periodic models, allow for the prediction of absolute BEs^{72,93} and can therefore be used to validate the relative BE shifts calculated using periodic models. Both models provide very similar results in terms of relative BE shifts, which is why once convergence with respect to model size was established⁷², the majority of calculations were conducted with periodic models via CASTEP.

Surface science experiments. A (110)-oriented single-crystal BDD sample (Element Six Ltd.) of size $5.00 \times 5.00 \times 0.47$ mm³ was homoepitaxially grown via microwave plasma CVD from a (110)-oriented SCD substrate. The growth chamber comprised a ~5% methane and hydrogen gas atmosphere at temperatures of 700–950 °C and pressures of 100–200 Torr, with microwave powers of 1–3 kW at 2.45 GHz¹⁹. The sample was highly boron-doped⁸ to low 10²⁰ atoms per cubic centimeter, and boron doping was achieved with the addition of up to 0.02% diborane(6) to the gas phase during CVD growth. A highly boron-doped sample was used to reduce charging effects within the XPS experiments, and the dopant concentration was low enough such that the surface termination of the diamond sample should not be affected⁹⁶. The sample was removed from the growth substrate via laser micromachining. A small amount of twinning was observed at the edge of the crystal, which both compromises the surface quality and can impact polishing. The twinning was removed by reducing the crystal size to $3.25 \times 3.25 \times 0.47$ mm³ using laser micromachining. To smooth the growth surface, the (110) surface was first mechanically lapped using a resin bonded wheel and then scribe cast iron polished. Prior to any analysis, the sample was acid-cleaned for 30 min at ~200 °C in concentrated sulfuric acid saturated with potassium nitrate, rinsed with deionized water, and cleaned again for 30 min at ~200 °C in concentrated sulfuric acid²³. The sample was finally ultrasonically cleaned for 15 min in deionized water and left to air-dry. All solutions were prepared from Milli-Q water (Millipore Corp.) with a resistivity of 18.2 M Ω cm at 25 °C.

The sample was characterized via XRD and LEED; full details for all experimental methods can be found in Supplementary Note 8. To obtain information about the surface roughness and morphology of the post-growth and polished crystal surface, AFM measurements were performed on different locations

of the surface using a Bruker Dimension Icon microscope operating in ScanAsystTM mode. The resulting AFM data were processed using the Gwyddion software⁹⁷.

XP spectra were recorded in an ultra-high vacuum with a 2×10^{-10} mbar base pressure. The sample was illuminated using an XM1000 monochromatic aluminum K_{α} X-ray source (Omicron NanoTechnology), corresponding to a 1486.7 eV photon energy. Photoelectrons were detected using a Sphera electron analyzer for two different electron emission angles, 0° and 60° with respect to the surface normal. The spectrometer work function was calibrated using a clean polycrystalline silver sample immediately prior to experiments commencing. The analyzer transmission function was calibrated using clean silver, gold, and copper foils. In order to remove any surface-adsorbed contaminants, the sample was annealed to different temperatures, with XPS measurements taken after every annealing step. An annealing temperature of 500 °C was found to be necessary to remove all contaminants whilst preventing decomposition of the surface oxide⁴⁹, as can be seen in Supplementary Fig. 12. XP spectra were fitted using symmetric pseudo-Voigt profiles^{98,99}, and if several peak components were present in a spectrum, they were restricted to have the same widths and Gaussian–Lorentzian ratios.

Data availability

Input and output files for all calculations have been uploaded as a dataset¹⁰⁰ to the NOMAD electronic structure data repository and are freely available under <https://doi.org/10.17172/NOMAD/2021.03.01-1>.

Code availability

Calculations and analysis have been performed with publicly available or licensed software.

Received: 1 June 2021; Accepted: 10 January 2022;

Published online: 28 January 2022

References

- Wooddell, C. E. Method of comparing the hardness of electric furnace products and natural abrasives. *Trans. Electrochem. Soc.* **68**, 111–130 (1935).
- Wei, L., Kuo, P. K., Thomas, R. L., Anthony, T. R. & Banholzer, W. F. Thermal conductivity of isotopically modified single crystal diamond. *Phys. Rev. Lett.* **70**, 3764–3767 (1993).
- Tohei, T., Kuwabara, A., Oba, F. & Tanaka, I. Debye temperature and stiffness of carbon and boron nitride polymorphs from first principles calculations. *Phys. Rev. B* **73**, 064304 (2006).
- Werner, M. & Locher, R. Growth and application of undoped and doped diamond films. *Rep. Prog. Phys.* **61**, 1665–1710 (1998).
- Wood, G. F., Terrero Rodriguez, I. M., Tully, J. J., Chaudhuri, S. & Macpherson, J. V. Electrochemical ozone generation using compacted high pressure high temperature synthesized boron doped diamond microparticle electrodes. *J. Electrochem. Soc.* **168**, 126514 (2021).
- Martineau, P. M. et al. High crystalline quality single crystal chemical vapour deposition diamond. *J. Phys. Condens. Matter* **21**, 364205 (2009).
- Jin, S. & Mavoori, H. Processing and properties of CVD diamond for thermal management. *J. Electron. Mater.* **27**, 1148–1153 (1998).
- Macpherson, J. V. A practical guide to using boron doped diamond in electrochemical research. *Phys. Chem. Chem. Phys.* **17**, 2935–2949 (2015).
- Yang, N. et al. Conductive diamond: Synthesis, properties, and electrochemical applications. *Chem. Soc. Rev.* **48**, 157–204 (2019).
- Brinza, O. et al. Dependence of CVD diamond growth rate on substrate orientation as a function of process parameters in the high microwave power density regime. *Phys. Status Solidi A* **205**, 2114–2120 (2008).
- Achard, J. et al. High quality MPACVD diamond single crystal growth: High microwave power density regime. *J. Phys. D Appl. Phys.* **40**, 6175–6188 (2007).
- Hartman, P. *Crystal growth: An introduction* (ed Hartman, P) 367–402 (North-Holland Publishing Company, 1973).
- Mackey, B. L. et al. Oxygen adsorption on the (110)-oriented diamond surface. *J. Phys. Chem. B* **105**, 3803–3812 (2001).
- Liu, D.-Q. et al. Facet-resolved electrochemistry of polycrystalline boron-doped diamond electrodes: Microscopic factors determining the solvent window in aqueous potassium chloride solutions. *ChemElectroChem* **5**, 3028–3035 (2018).
- Hussein, H. E. M. et al. Tracking metal electrodeposition dynamics from nucleation and growth of a single atom to a crystalline nanoparticle. *ACS Nano* **12**, 7388–7396 (2018).
- Friel, I. et al. Control of surface and bulk crystalline quality in single crystal diamond grown by chemical vapour deposition. *Diam. Relat. Mater.* **18**, 808–815 (2009).
- Badzian, A. & Badzian, T. Diamond homoepitaxy by chemical vapor deposition. *Diam. Relat. Mater.* **2**, 147–157 (1993).

18. Silva, F. et al. Geometric modeling of homoepitaxial CVD diamond growth: I. The {100}{111}{110}{113} system. *J. Cryst. Growth* **310**, 187–203 (2008).
19. Balmer, R. S. et al. Chemical vapour deposition synthetic diamond: Materials, technology, and applications. *J. Phys. Condens. Matter* **21**, 364221 (2009).
20. Martin, H. B., Argoitia, A., Landau, U., Anderson, A. B. & Angus, J. C. Hydrogen and oxygen evolution on boron-doped diamond electrodes. *J. Electrochem. Soc.* **143**, L133–L136 (1996).
21. Yagi, I., Notsu, H., Kondo, T., Tryk, D. A. & Fujishima, A. Electrochemical selectivity for redox systems at oxygen-terminated diamond electrodes. *J. Electroanal. Chem.* **473**, 173–178 (1999).
22. Maier, F., Ristein, J. & Ley, L. Electron affinity of plasma-hydrogenated and chemically oxidized diamond (100) surfaces. *Phys. Rev. B* **143**, 165411 (2001).
23. Hutton, L. A. et al. Examination of the factors affecting the electrochemical performance of oxygen-terminated polycrystalline boron-doped diamond electrodes. *Anal. Chem.* **85**, 7230–7240 (2013).
24. Fischer, A. E., Show, Y. & Swain, G. M. Electrochemical performance of diamond thin-film electrodes from different commercial sources. *Anal. Chem.* **76**, 2553–2560 (2004).
25. Liu, F. B., Wang, J. D., Liu, B., Li, X. M. & Chen, D. R. Effect of electronic structures on electrochemical behaviors of surface-terminated boron-doped diamond film electrodes. *Diam. Relat. Mater.* **16**, 454–460 (2007).
26. Cui, S. & Hu, E. L. Increased negatively charged nitrogen-vacancy centers in fluorinated diamond. *Appl. Phys. Lett.* **103**, 051603 (2013).
27. Meara, C. J., Rayson, M. J., Briddon, P. R. & Goss, J. P. A computational study of nanodiamond surface radicals and nitrogen-vacancy charge fluctuations. *J. Phys. Chem. Solids* **146**, 109637 (2020).
28. Santori, C. et al. Nanophotonics for quantum optics using nitrogen-vacancy centers in diamond. *Nanotechnology* **21**, 274008 (2010).
29. Nizovtsev, A. P. et al. A quantum computer based on NV centers in diamond: Optically detected nutations of single electron and nuclear spins. *Opt. Spectrosc.* **99**, 233–244 (2005).
30. Dutt, M. V. G. et al. Quantum register based on individual electronic and nuclear spin qubits in diamond. *Science* **316**, 1312–1316 (2007).
31. Neumann, P. et al. Multiparticle entanglement among single spins in diamond. *Science* **320**, 1326–1329 (2008).
32. Loh, K. P., Xie, X. N., Yang, S. W. & Zheng, J. C. Oxygen adsorption on (111)-oriented diamond: A study with ultraviolet photoelectron spectroscopy, temperature-programmed desorption, and periodic density functional theory. *J. Phys. Chem. B* **106**, 5230–5240 (2002).
33. Zheng, J., Xie, X. N., Wee, A. T. S. & Loh, K. P. Oxygen-induced surface state on diamond (100). *Diamond Relat. Mater.* **10**, 500–505 (2001).
34. Whitten, J. L., Cremaschi, P., Thomas, R. E., Rudder, R. A. & Markunas, R. J. Effects of oxygen on surface reconstruction of carbon. *Appl. Surf. Sci.* **75**, 45–50 (1994).
35. Zheng, X. M. & Smith, P. V. The stable configurations for oxygen chemisorption on the diamond (100) and (111) surfaces. *Surf. Sci.* **262**, 219–234 (1992).
36. Tamura, H. et al. Periodic density-functional study on oxidation of diamond (100) surfaces. *Phys. Rev. B* **61**, 11025–11033 (2000).
37. Skokov, S., Weiner, B. & Frenklach, M. Molecular-dynamics study of oxygenated (100) diamond surfaces. *Phys. Rev. B* **49**, 11374–11382 (1993).
38. Petrini, D. & Larsson, K. A theoretical study of the energetic stability and geometry of hydrogen- and oxygen-terminated diamond (100) surfaces. *J. Phys. Chem. C* **111**, 795–801 (2007).
39. Derry, T. E., Makau, N. W. & Stampf, C. Oxygen adsorption on the (1 × 1) and (2 × 1) reconstructed C(111) surfaces: a density functional theory study. *J. Phys. Condens. Matter* **22**, 265007 (2010).
40. Larsson, K. The combined influence of dopant species and surface termination on the electronic properties of diamond surfaces. *C.* **6**, 22 (2020).
41. Hassan, M. M. & Larsson, K. Effect of surface termination on diamond (100) surface electrochemistry. *J. Phys. Chem. C* **118**, 22995–23002 (2014).
42. Wan, G., Cattelan, M. & Fox, N. A. Electronic structure tunability of diamonds by surface functionalization. *J. Phys. Chem. C* **123**, 4168–4177 (2019).
43. Struck, L. M. & D'Evelyn, M. P. Interaction of hydrogen and water with diamond (100): Infrared spectroscopy. *J. Vac. Sci. Technol. A* **11**, 1992–1997 (1993).
44. Pehrsson, P. E. & Mercer, T. W. Oxidation of the hydrogenated diamond (100) surface. *Surf. Sci.* **460**, 49–66 (2000).
45. Pehrsson, P. E. & Mercer, T. W. Oxidation of heated diamond C(100):H surfaces. *Surf. Sci.* **460**, 74–90 (2000).
46. Takeuchi, D., Ri, S.-G., Tokuda, N. & Yamasaki, S. Recovery of negative electron affinity by annealing on (111) oxidized diamond surfaces. *Diam. Relat. Mater.* **18**, 206–209 (2009).
47. Makau, N. W. & Derry, T. E. Study of oxygen on the three low index diamond surfaces by XPS. *Surf. Rev. Lett.* **10**, 295–301 (2003).
48. Baldwin, C. G., Downes, J. E., McMahon, C. J., Bradac, C. & Mildren, R. P. Nanostructuring and oxidation of diamond by two-photon ultraviolet surface excitation: An XPS and NEXAFS study. *Phys. Rev. B* **89**, 195422 (2014).
49. Bobrov, K., Shechter, H., Hoffman, A. & Folman, M. Molecular oxygen adsorption and desorption from single crystal diamond (111) and (110) surfaces. *Appl. Surf. Sci.* **196**, 173–180 (2002).
50. Mercer, T. W., Russell, J. N. & Pehrsson, P. E. The effect of a hydrogen plasma on the diamond (110) surface. *Surf. Sci.* **392**, L21–L26 (1997).
51. Hohenberg, P. & Kohn, W. Inhomogeneous electron gas. *Phys. Rev.* **136**, B864–B871 (1964).
52. Kohn, W. & Sham, L. Self-consistent equations including exchange and correlation effects. *Phys. Rev.* **140**, A1133–A1138 (1965).
53. Reuter, K. & Scheffler, M. Composition, structure, and stability of RuO₂(110) as a function of oxygen pressure. *Phys. Rev. B* **65**, 035406 (2001).
54. Reuter, K. & Scheffler, M. Composition and structure of the RuO₂(110) surface in an O₂ and CO environment: Implications for the catalytic formation of CO₂. *Phys. Rev. B* **68**, 045407 (2003).
55. Reuter, K., Stampf, C. & Scheffler, M. *Handbook of Materials Modeling* (ed Yip, S.) 149–194 (Springer, 2005).
56. Perdew, J. P., Burke, K. & Ernzerhof, M. Generalized gradient approximation made simple. *Phys. Rev. Lett.* **77**, 3865–3868 (1996).
57. Maurer, R. J. et al. Advances in density-functional calculations for materials modeling. *Annu. Rev. Mater. Sci.* **49**, 1–30 (2019).
58. Perdew, J. P., Ruzsinszky, A., Constantin, L. A., Sun, J. & Csonka, G. I. Some fundamental issues in ground-state density functional theory: A guide for the perplexed. *J. Chem. Theory Comput.* **5**, 902–908 (2009).
59. Hofmann, O. T., Zojer, E., Hörmann, L., Jeindl, A. & Maurer, R. J. First-principles calculations of hybrid inorganic-organic interfaces: From state-of-the-art to best practice. *Phys. Chem. Chem. Phys.* **23**, 8132–8180 (2021).
60. Zhang, Y. & Yang, W. Comment on “Generalized gradient approximation made simple”. *Phys. Rev. Lett.* **80**, 890 (1998).
61. Hammer, B., Hansen, L. B. & Nørskov, J. K. Improved adsorption energetics within density-functional theory using revised Perdew-Burke-Ernzerhof functionals. *Phys. Rev. B* **59**, 7413–7421 (1999).
62. Becke, A. D. Density-functional exchange-energy approximation with correct asymptotic behavior. *Phys. Rev. A* **38**, 3098–3100 (1988).
63. Lee, C., Yang, W. & Parr, R. G. Development of the Colle-Salvetti correlation-energy formula into a functional of the electron density. *Phys. Rev. B* **37**, 785–789 (1988).
64. Tao, J., Perdew, J. P., Staroverov, V. N. & Scuseria, G. E. Climbing the density functional ladder: Nonempirical meta-generalized gradient approximation designed for molecules and solids. *Phys. Rev. Lett.* **91**, 14601 (2003).
65. Goedecker, S. Minima hopping: An efficient search method for the global minimum of the potential energy surface of complex molecular systems. *J. Chem. Phys.* **120**, 9911–9917 (2004).
66. Peterson, A. A. Global optimization of adsorbate-surface structures while preserving molecular identity. *Top. Catal.* **57**, 40–53 (2014).
67. Larsen, A. H. et al. The atomic simulation environment—a Python library for working with atoms. *J. Phys. Condens. Matter* **29**, 273002 (2017).
68. Bundy, F. P. et al. The pressure-temperature phase and transformation diagram for carbon; updated through 1994. *Carbon* **34**, 141–153 (1996).
69. Cobb, S. J. et al. Assessment of acid and thermal oxidation treatments for removing sp² bonded carbon from the surface of boron doped diamond. *Carbon* **167**, 1–10 (2020).
70. Kononenko, V. V. et al. Effect of the pulse duration on graphitisation of diamond during laser ablation. *Quant. Electron.* **35**, 252–256 (2005).
71. Osswald, S., Yushin, G., Mochalin, V., Kucheyev, S. O. & Gogotsi, Y. Control of sp²/sp³ carbon ratio and surface chemistry of nanodiamond powders by selective oxidation in air. *J. Am. Chem. Soc.* **128**, 11635–11642 (2006).
72. Klein, B. P., Hall, S. J. & Maurer, R. J. The nuts and bolts of ab-initio core-hole simulations for K-shell X-ray photoemission and absorption spectra. *J. Phys. Condens. Matter* **33**, 154005 (2021).
73. Musket, R. G., McLean, W., Colmenares, C. A., Makowiecki, D. M. & Siekhaus, W. J. Preparation of atomically clean surfaces of selected elements: A review. *Appl. Surf. Sci.* **10**, 143–207 (1982).
74. Barr, T. L. & Seal, S. Nature of the use of adventitious carbon as a binding energy standard. *J. Vac. Sci. Technol. A* **13**, 1239–1246 (1995).
75. Swift, P. Adventitious carbon—the panacea for energy referencing? *Surf. Interface Anal.* **4**, 47–51 (1982).
76. Miller, D. J., Biesinger, M. C. & McIntyre, N. S. Interactions of CO₂ and CO at fractional atmosphere pressures with iron and iron oxide surfaces: One possible mechanism for surface contamination? *Surf. Interface Anal.* **33**, 299–305 (2002).
77. Barr, T. L. & Seal, S. Practical guides for X-ray photoelectron spectroscopy (XPS): Interpreting the carbon 1s spectrum. *J. Vac. Sci. Technol. A* **39**, 013204 (2021).
78. Nishitani-Gamo, M. et al. Surface morphology of homoepitaxially grown (111), (001), and (110) diamond studied by low energy electron diffraction and reflection high-energy electron diffraction. *J. Vac. Sci. Technol. A* **17**, 2991–3002 (1999).
79. Maier, F. et al. The hydrogenated and bare diamond (110) surface: A combined LEED-, XPS-, and ARPES study. *Surf. Sci.* **443**, 177–185 (1999).

80. Bobrov, K., Shechter, H., Folman, M. & Hoffman, A. A study of deuterium interaction with diamond (110) single crystal surface by TPD, EELS, and LEED. *Diam. Relat. Mater.* **8**, 705–711 (1999).
81. Sutcu, L. F. et al. Atomic force microscopy of (100), (110), and (111) homoepitaxial diamond films. *J. Appl. Phys.* **71**, 5930–5940 (1992).
82. Blum, V. et al. Ab initio molecular simulations with numeric atom-centered orbitals. *Comput. Phys. Commun.* **180**, 2175–2196 (2009).
83. Havu, V., Blum, V., Havu, P. & Scheffler, M. Efficient O(N) integration for all-electron electronic structure calculation using numeric basis functions. *J. Comput. Phys.* **228**, 8367–8379 (2009).
84. Knuth, F., Carbogno, C., Atalla, V., Blum, V. & Scheffler, M. All-electron formalism for total energy strain derivatives and stress tensor components for numeric atom-centered orbitals. *Comput. Phys. Commun.* **190**, 33–50 (2015).
85. Marek, A. et al. The ELPA library: Scalable parallel eigenvalue solutions for electronic structure theory and computational science. *J. Phys. Condens. Matter* **26**, 213201 (2014).
86. Yu, V. W.-z et al. ELSI: A unified software interface for Kohn–Sham electronic structure solvers. *Comput. Phys. Commun.* **222**, 267–285 (2018).
87. Tkatchenko, A. & Scheffler, M. Accurate molecular van Der waals interactions from ground-state electron density and free-atom reference data. *Phys. Rev. Lett.* **102**, 073005 (2009).
88. Chase, M. W. NIST-JANAF thermochemical tables. *J. Chem. Phys. Ref. Data* **9**, 1–1951 (1998).
89. Jones, R. O. & Gunnarsson, O. The density functional formalism, its applications, and prospects. *Rev. Mod. Phys.* **61**, 689–746 (1989).
90. Hellman, A., Razaznejad, B. & Lundqvist, B. I. Potential-energy surfaces for excited states in extended systems. *J. Chem. Phys.* **120**, 4593–4602 (2004).
91. Clark, S. et al. First principles methods using CASTEP. *Z. Kristallogr.* **220**, 567–570 (2005).
92. Mizoguchi, T., Tanaka, I., Gao, S.-P. & Pickard, C. J. First-principles calculation of spectral features, chemical shift and absolute threshold of ELNES and XANES using a plane wave pseudopotential method. *J. Phys. Condens. Matter* **21**, 104204 (2009).
93. Kahk, J. M. & Lischner, J. Accurate absolute core-electron binding energies of molecules, solids, and surfaces from first-principles calculations. *Phys. Rev. Mater.* **3**, 100801(R) (2019).
94. Lu, Y. et al. Open-source, Python-based redevelopment of the ChemShell multiscale QM/MM environment. *J. Chem. Theory Comput.* **15**, 1317–1328 (2019).
95. Mulliken, R. S. Electronic population analysis on LCAO-MO molecular wave functions. I. *J. Chem. Phys.* **23**, 1833–1840 (1955).
96. Quaino, P. M. & Schmickler, W. Oxygen-terminated diamond electrodes in alkaline media: Structure and OH generation. *ChemElectroChem* **1**, 933–939 (2014).
97. Nečas, D. & Klapetek, P. Gwyddion: An open-source software for SPM data analysis. *Cent. Eur. J. Phys.* **10**, 181–188 (2012).
98. Schmid, M., Steinrück, H.-P. & Gottfried, J. M. A new asymmetric Pseudo-Voigt function for more efficient fitting of XPS lines. *Surf. Interface Anal.* **46**, 505–511 (2014).
99. Schmid, M., Steinrück, H.-P. & Gottfried, J. M. A new asymmetric Pseudo-Voigt function for more efficient fitting of XPS lines. *Surf. Interface Anal.* **47**, 1080 (2015).
100. Chaudhuri, S., Hall, S. J., Klein, B. P. & Maurer, R. J. Oxygen on Diamond(110) dataset. <https://doi.org/10.17172/NOMAD/2021.03.01-1> (2021).

Acknowledgements

This work was funded by the EPSRC Center for Doctoral Training in Diamond Science and Technology [EP/L015315/1] (S.C.), the EPSRC Center for Doctoral Training in Molecular Analytical Science [EP/L015307/1] (S.J.H.), the Deutsche Forschungsgemeinschaft [KL 3430/1-1] (B.P.K.), the UKRI Future Leaders Fellowship program [MR/T018372/1 and MR/S016023/1] (A.J.L. and R.J.M. respectively) and the EPSRC Engineered Diamond Tech-

nologies program [EP/V056778/1] (J.V.M.). Computing resources were provided by the Scientific Computing Research Technology Platform of the University of Warwick (including access to Orac and Tinis), the EPSRC-funded HPC Midlands+ consortium [EP/P020232/1] for access to Athena, and the EPSRC-funded High End Computing Materials Chemistry Consortium [EP/R029431/1] for access to the ARCHER UK National Supercomputing Service (<https://www.archer.ac.uk>) and the ARCHER2 UK National Supercomputing Service (<https://www.archer2.ac.uk>). The SCD was grown by Nicola Palmer (Element Six Ltd.) and polished by Adam Rathmill (Technical Diamond Polishing Ltd.). XPS and LEED measurements were conducted at the Warwick Photoemission Research Technology Platform, and AFM measurements were conducted at the Electron Microscopy Research Technology Platform of the University of Warwick, with thanks to Pei Zhao (Department of Chemistry, University of Warwick) for Gwyddion analysis. XRD measurements were conducted at the X-Ray Diffraction Research Technology Platform of the University of Warwick by David Walker (Department of Physics, University of Warwick). We also thank Claire Hurley, Steve Hindmarsh, and Mark Newton (Department of Physics, University of Warwick) for helpful discussions during the AFM and XPS measurements. Correspondence to R.J.M. and J.V.M.

Author contributions

R.J.M. and J.V.M. conceived and designed this research. S.C. and S.J.H. performed all calculations and A.J.L. contributed to the cluster calculations. B.P.K., M.W., and J.V.M. performed the surface science experiments. R.J.M., S.C., S.J.H., B.P.K., and J.V.M. interpreted all the data. S.C., R.J.M., and J.V.M. wrote the manuscript with substantial contributions by S.J.H. and B.P.K. All authors commented on the manuscript.

Competing interests

R.J.M. is an Editorial Board Member for *Communications Materials* and was not involved in the editorial review of, or the decision to publish, this article. All other authors declare no competing interests.

Additional information

Supplementary information The online version contains supplementary material available at <https://doi.org/10.1038/s43246-022-00228-4>.

Correspondence and requests for materials should be addressed to Julie V. Macpherson or Reinhard J. Maurer.

Peer review information *Communications Materials* thanks the anonymous reviewers for their contribution to the peer review of this work. Primary Handling Editor: Aldo Isidori. Peer reviewer reports are available.

Reprints and permission information is available at <http://www.nature.com/reprints>

Publisher's note Springer Nature remains neutral with regard to jurisdictional claims in published maps and institutional affiliations.



Open Access This article is licensed under a Creative Commons Attribution 4.0 International License, which permits use, sharing, adaptation, distribution and reproduction in any medium or format, as long as you give appropriate credit to the original author(s) and the source, provide a link to the Creative Commons license, and indicate if changes were made. The images or other third party material in this article are included in the article's Creative Commons license, unless indicated otherwise in a credit line to the material. If material is not included in the article's Creative Commons license and your intended use is not permitted by statutory regulation or exceeds the permitted use, you will need to obtain permission directly from the copyright holder. To view a copy of this license, visit <http://creativecommons.org/licenses/by/4.0/>.

© The Author(s) 2022